

Article

# Sensorless Control Strategy of Novel Axially Magnetized Vernier Permanent-Magnet Machine

Bowen Xu , Jien Ma <sup>\*</sup>, Qiyi Wu , Lin Qiu , Xing Liu, Chao Luo and Youtong Fang

College of Electrical Engineering, Zhejiang University, Hangzhou 310027, China; xbwen@zju.edu.cn (B.X.); kiwuwu@zju.edu.cn (Q.W.); qiu\_lin@zju.edu.cn (L.Q.); xingldl@zju.edu.cn (X.L.); luochao@zju.edu.cn (C.L.); youtong@zju.edu.cn (Y.F.)

\* Correspondence: majien@zju.edu.cn; Tel.: +86-137-5716-1686

**Abstract:** Vernier permanent-magnet machines have been attracted more and more attention because of their high torque density. In this paper, the sensorless control strategy of the novel axially magnetized Vernier permanent-magnet (AMVPM) machine is presented. First, the inductance non-linearity is investigated under different load conditions. Second, the mathematical model is established in cooperation with the finite element method. After that, the back electromotive force based sensorless control strategy is developed according to the state equation of the motor. In the sensorless drive, the model reference adaptive system (MRAS) technique incorporated with the inductance non-linearity is used for the speed estimation. The modified control strategy not only increases the stability but also improves the dynamic response of the system. Finally, the simulation results show that the modified MRAS is of high estimation precision, and the AMVPM machine can be well controlled, and the experimental results validated the theoretical design process.

**Keywords:** model reference adaptive system; permanent-magnet machine; vector control; Vernier machine



**Citation:** Xu, B.; Ma, J.; Wu, Q.; Qiu, L.; Liu, X.; Luo, C.; Fang, Y. Sensorless Control Strategy of Novel Axially Magnetized Vernier Permanent-Magnet Machine. *Energies* **2022**, *15*, 5470. <https://doi.org/10.3390/en15155470>

Academic Editors: Lorand Szabo and Christopher H. T. Lee

Received: 16 June 2022

Accepted: 25 July 2022

Published: 28 July 2022

**Publisher's Note:** MDPI stays neutral with regard to jurisdictional claims in published maps and institutional affiliations.



**Copyright:** © 2022 by the authors. Licensee MDPI, Basel, Switzerland. This article is an open access article distributed under the terms and conditions of the Creative Commons Attribution (CC BY) license (<https://creativecommons.org/licenses/by/4.0/>).

## 1. Introduction

Vernier permanent-magnet (VPM) machines have attracted considerable attentions in recent years. It is found that VPM machines have inherent characteristic called magnetic gearing effect, which brings the topologies many benefits, such as high power density, high efficiency, and direct-driving. These advantages make VPM machines a promising candidate in many applications, such as wind power generation, vehicle propulsion, and robotic servo system. The industrial application prospect of VPM machines makes it a research interest in recent years, during which many works have been completed [1–5].

However, the VPM machines with rotor surface-mounted PMs usually have weak mechanical strength. When working in adverse conditions, a sleeve needs to be used on the rotor to reinforce the rotor structure. The adoption of the sleeve complicates the installation process and increases the air-gap width. To solve this problem, researchers focus on the stator-PM structures to enhance the rotor robustness [6–14]. However, among them, the doubly-salient machines [6–8] have quite low torque density and large torque ripple. Additionally, the core lamination shapes of flux-reversal machines [9–11] and switched-flux machines [12–14] are complex, which makes the fabrication and assembly process very difficult.

To this end, a novel axially magnetized VPM (AMVPM) machine structure is proposed [15,16]. The structure installed the PMs directly on the axis to enhance the mechanical strength. The finite element analysis (FEA) and experiment results show that the structure can produce 12.8% larger torque with 22.6% less PM usage compared with regular VPM machine. The expected application for the proposed machine is in a submersible environment, where the position sensor is not recommended. Therefore, it is desirable to use the sensorless control strategy to further improve the performance of the machine.

The sensorless vector control strategies [17–27] can be preliminarily divided into signal injection method [17–19] and back-EMF-based method [20–28]. Among them, the

back-EMF-based method is suitable for middle-speed working conditions, and it has been extensively developed in recent years. In order to solve the problem of motor parameters variation, the state observer has been proposed and thoroughly discussed. The state observer mainly includes model reference adaptive system (MRAS) [20–22], artificial neural network [23], extended Kalman filter [24], sliding-mode controller [25], full/reduced order observer [26,27], and extended back-EMF method [28]. Among them, the MRAS method is singled out as having less computing time, easy implementation, and straightforward stability approach.

Motivated by the above observations, in this paper, a modified MRAS online identification method for AMVPM machine is developed as the speed estimation method in the back electromotive force based sensorless control strategy. Meanwhile, the relevant electromagnetic parameters of AMVPM machine is investigated by the FEA method in advance. The inductance non-linearity is investigated under different load conditions. In this way, the accuracy of the reference model can be improved, so the estimation accuracy of the MRAS technique can be enhanced. The main contributions of this paper is: (a) to improve the MRAS speed estimator by incorporating with the non-linear stator inductance calculation table, which is established by FEA method in advance; (b) to demonstrate the feasibility of using MRAS-based sensorless control method to control the AMVPM machine; (c) to apply the improved MRAS-based sensorless control strategy to the AMVPM machine for the first time; and (d) to evaluate the performances of the proposed strategy for AMVPM machine by simulation method in various operating conditions and verify the theoretical analysis results of full paper by experimental validation.

This paper is organized as follows. In Section 2, the structure and operation principle of the proposed machine are demonstrated. In Section 3, the inductance matrix is modeled by the FEA method. In Section 4, the sensorless control system including the MRAS estimation is designed. In Section 5, the simulation results are discussed. Section 6 includes the manufacturing and testing process of the machine prototype to confirm the theoretical analysis. Section 7 concludes this paper.

## 2. Machine Structure and Operation Principle

The structure of AMVPM machine is shown in Figure 1. As can be seen, the PMs are magnetized along the axis alternately and sandwiched between the rotor and the end caps. In this way, the PMs can be fixed directly on the axis and rotate with it, which can improve the mechanical strength and simplify the machining process. The stator is a conventional open-slot structure.

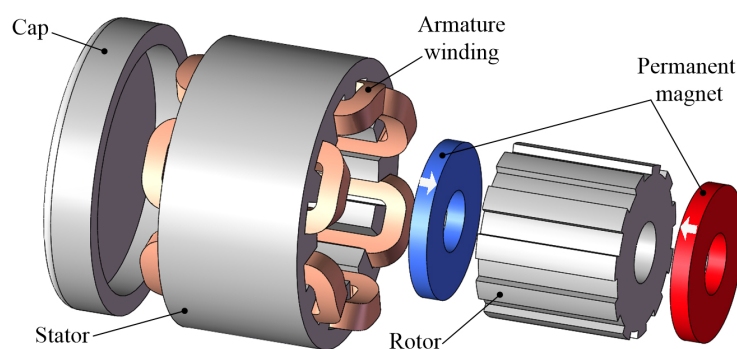


**Figure 1.** Structure of the axially magnetized VPM machine.

The flux lines distribution is shown in Figure 2. It can be found in the front view (left) that the flux lines come from N-pole of the PMs, pass through the rotor, the air-gap, the stator, the cap, and return to S-pole of the PMs. Therefore, in the top view (right), the flux lines radiate from the rotor and converge at the stator. In this paper, a 12-stator-slot/7-rotor-pole topology is selected as the study objective. The detailed mechanical parameters are given in Table 1.

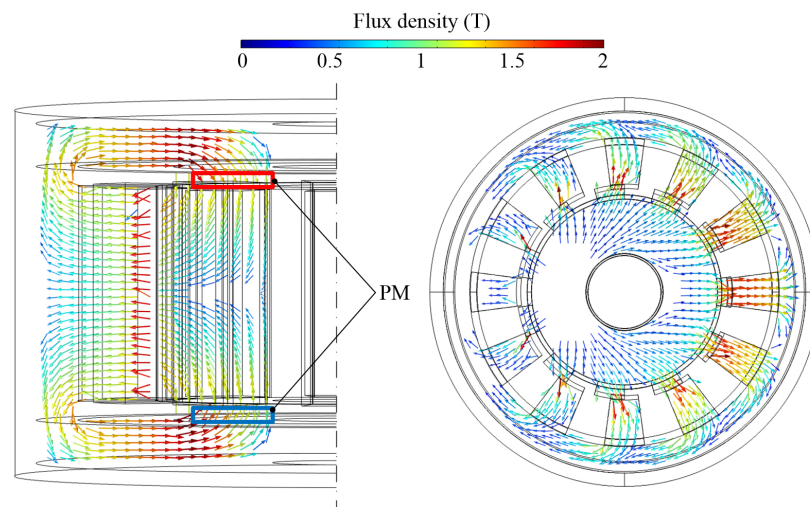


**Figure 2.** Magnetic field profile distribution of the proposed machine.

**Table 1.** Design Parameters of the Proposed Machine.

Parameters	Value
Stator outer diameter	140 mm
Split ratio	0.6
Stator slot number	12
Rotor slot number	7
Air-gap length	1 mm
Core length	50 mm
PM thickness	9 mm
PM type	NMX-S38EH (60 °C)
Silicon steel type	35WW400

In order to establish the state equation of the machine, some of the electromagnetic parameters will be investigated in this section. It should be noted that the temperature will influence not only resistance but also characteristic curve of the PM, and the machine loss and temperature variation are both unmeasurable. Therefore, the analysis in this paper is based on the assumption that the temperature is fixed.

According to [29], the permeance density of one-side slotted structure can be expressed as

$$\Lambda(\theta) = \Lambda_0 + \sum_{k=1}^{\infty} \Lambda_k \cos(kZ\theta), \quad (1)$$

where

$$\Lambda_0 = \frac{\mu_0}{g} (1 - 1.6\beta c_0), \quad (2)$$

$$\Lambda_k = \frac{2\mu_0\beta}{k\pi g} \frac{0.78}{0.78 - 2c_0^2} \sin(1.6k\pi c_0), \quad (3)$$

$$\beta = \frac{1}{2} \left( 1 - \frac{1}{\sqrt{1 + \left(\frac{o}{2g}\right)^2}} \right), \quad (4)$$

$$c_0 = \frac{o}{t_d}, \quad (5)$$

where  $\mu_0$  represents the permeability of vacuum,  $Z$  represents the teeth number,  $g$  represents the air-gap length,  $o$  represents the slot opening width, and  $t_d$  represents the slot pitch. It is noted that, for a well optimized topology, the slot depth can be neglected.

Therefore, the one-side permeance density of stator and rotor can be separately expressed as

$$\Lambda_s(\theta_s) = \Lambda_{s0} + \sum_{i=1}^{\infty} \Lambda_{si} \cos(iZ_s \theta_s), \quad (6)$$

$$\Lambda_r(\theta_r) = \Lambda_{r0} + \sum_{j=1}^{\infty} \Lambda_{rj} \cos(jZ_r \theta_r). \quad (7)$$

The permeance density of doubly salient structure can be calculated as [30]

$$\Lambda_g(\theta) \approx \Lambda_s(\theta) \Lambda_r(\theta - \theta_0) / \frac{\mu_0}{g}. \quad (8)$$

Substituting (6) and (7) into (8), one can obtain:

$$\begin{aligned} \Lambda_g(\theta) &= \Lambda_{s0} \Lambda_{r0} + \Lambda_{r0} \sum_{i=1}^{\infty} \Lambda_{si} \cos(iZ_s \theta) + \Lambda_{s0} \sum_{j=1}^{\infty} \Lambda_{rj} \cos(jZ_r (\theta - \omega_m t)) \\ &+ \sum_{i=1}^{\infty} \sum_{j=1}^{\infty} \Lambda_{si} \Lambda_{rj} \cos(iZ_s \theta + jZ_r (\theta - \omega_m t)) + \sum_{i=1}^{\infty} \sum_{j=1}^{\infty} \Lambda_{si} \Lambda_{rj} \cos(iZ_s \theta - jZ_r (\theta - \omega_m t)). \end{aligned} \quad (9)$$

The air-gap radial flux density can be written as

$$B(\theta) = F \cdot \Lambda(\theta), \quad (10)$$

where F is the magnetic potential difference.

Table 1 shows that in the proposed machine,  $Z_s$  is 12 and  $Z_r$  is 7. According to the magnetic gearing effect, the pole pair number of armature winding is  $(Z_s - Z_r) = 5$ . Thus, the one-phase stator flux linkage can be expressed as

$$\begin{aligned} \psi &= N_{ph} l_{stk} R_g \left( \int_{-\frac{\pi}{Z_s}}^{\frac{\pi}{Z_s}} F \Lambda(\theta) d\theta - \int_{\pi - \frac{\pi}{Z_s}}^{\pi + \frac{\pi}{Z_s}} F \Lambda(\theta) d\theta \right) \\ &= 2N_{ph} l_{stk} R_g \left( \sum_{j=1,3,5,\dots}^{\infty} \frac{2\Lambda_{s0} \Lambda_{rj}}{jZ_r} \cos(jZ_r \omega_m t) \sin(j \frac{Z_r}{Z_s} \pi) \right. \\ &+ \sum_{i=1}^{\infty} \sum_{j=1,3,5,\dots}^{\infty} \frac{\Lambda_{si} \Lambda_{rj}}{iZ_s + jZ_r} \cos(jZ_r \omega_m t) \sin(i\pi + j \frac{Z_r}{Z_s} \pi) + \sum_{i=1}^{\infty} \sum_{j=1,3,5,\dots}^{\infty} \frac{\Lambda_{si} \Lambda_{rj}}{iZ_s - jZ_r} \cos(jZ_r \omega_m t) \sin(i\pi - j \frac{Z_r}{Z_s} \pi) \left. \right). \end{aligned} \quad (11)$$

The one-phase back-EMF can be expressed as

$$\begin{aligned} E &= \frac{d\psi}{dt} = -2N_{ph} l_{stk} R_g \omega_m \left( \sum_{j=1,3,5,\dots}^{\infty} 2\Lambda_{s0} \Lambda_{rj} \sin(j \frac{Z_r}{Z_s} \pi) \right. \\ &+ \sum_{i=1}^{\infty} \sum_{j=1,3,5,\dots}^{\infty} \Lambda_{si} \Lambda_{rj} \frac{jZ_r}{iZ_s} \frac{\sin(1 + \frac{jZ_r}{iZ_s}) i\pi}{(1 + \frac{jZ_r}{iZ_s})} + \sum_{i=1}^{\infty} \sum_{j=1,3,5,\dots}^{\infty} \Lambda_{si} \Lambda_{rj} \frac{jZ_r}{iZ_s} \frac{\sin(1 - \frac{jZ_r}{iZ_s}) i\pi}{(1 - \frac{jZ_r}{iZ_s})} \left. \right) \sin(jZ_r \omega_m t). \end{aligned} \quad (12)$$

Substituting (3) into (12), the amplitude of each order of back-EMF harmonic is shown in Figure 3. The amplitude has been normalized based on the fundamental component value. As can be seen, all the high order harmonic amplitudes are less than 0.08. The analytical results show that the proposed machine has the potential to produce sinusoidal back-EMF. The FEA results also proved the conclusion, as can be seen in Figure 4. The open-circuit back-EMF wave in A-phase coils is very sinusoidal. Additionally, the accuracy of analytical result is proved to be very high. The cogging torque is naturally small because the LCM of stator and rotor poles are very large. As shown in Figure 5, the amplitude of cogging torque is under 0.05 Nm. Therefore, it is concluded that when the phase current is also sinusoidal, the proposed machine has the capacity to produce constant torque, which is the basic function of a vector control system.

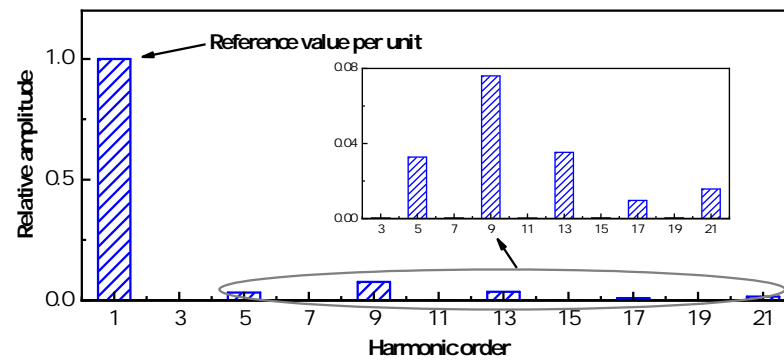


**Figure 3.** Relationship between normalized amplitude of harmonic component in back-EMF with its order.

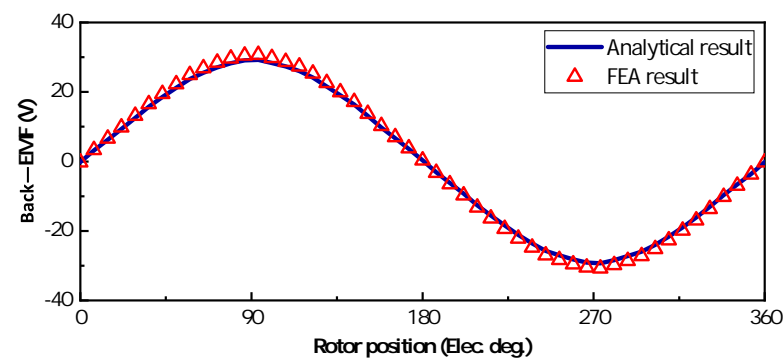


**Figure 4.** Comparison between FEA and analytical results of induced back-EMF.

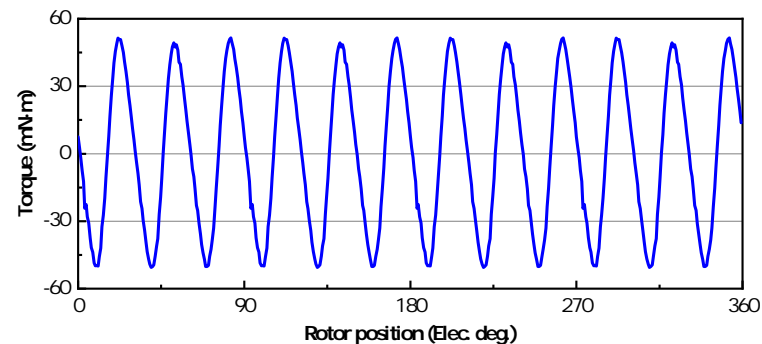


**Figure 5.** Relationship between cogging torque and rotor position.

### 3. Inductance Matrix Modeling

The estimation accuracy of the MRAS method is directly affected by the parameter accuracy of the reference model itself. However, in the process of machine design, in order to improve the performance of the motor as much as possible, there will be saturation in the iron core. It causes the stator inductance to be always changing during the operation of the motor. In order to improve the precision of the sensorless speed estimation, the induction matrix under a series of load conditions is calculated by FEA software in advance. In the real-time operation process, the d-axis and q-axis inductance will be calculated by the look-up table.

The calculated  $L_d$  and  $L_q$  under a set of  $i_d$  and  $i_q$  are shown in Figure 6. As can be seen, in general, the inductance decreases when the current increases. Considering that  $i_d$  is the field current, and  $i_q$  is the torque current, the range of  $i_d$  is  $-10\sim 10$  A and the range of  $i_q$  is  $0\sim 20$  A.

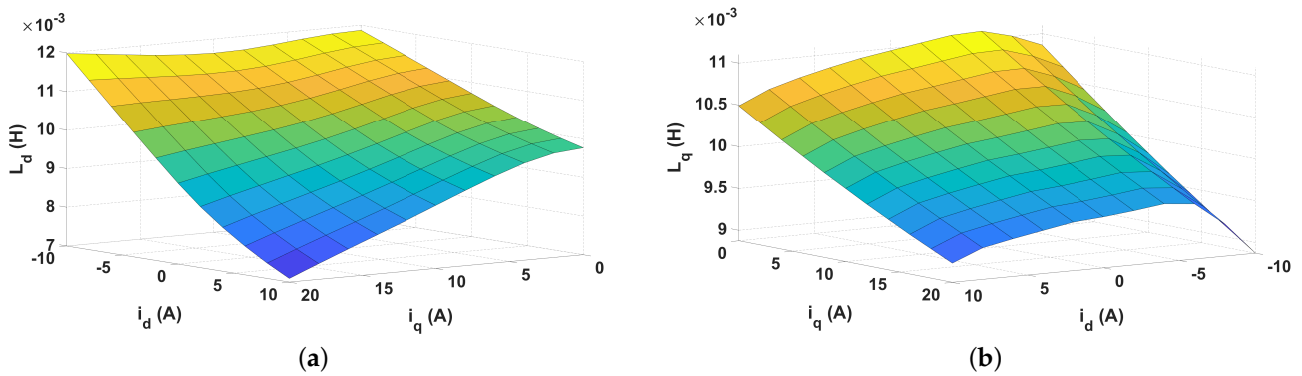


Figure 6. The relationship between inductance and  $(i_d, i_q)$ . (a)  $L_d$ ; (b)  $L_q$ .

Additionally, the excitation field generated by the PMs needs to be obtained to complete the state equation. Through FEA method, the three phase open-circuit flux linkage is shown in Figure 7. Since the constant amplitude transformation method is adopted in the control process, the value of  $\psi_f$  is 67.38 mWb.

After the stator resistance measured by the RLC testing device, the the state space model of the proposed AMVPM machine can be established.

$$\begin{bmatrix} \psi_d \\ \psi_q \end{bmatrix} = \begin{bmatrix} L_d(i_d, i_q) & 0 \\ 0 & L_q(i_d, i_q) \end{bmatrix} \begin{bmatrix} i_d \\ i_q \end{bmatrix} + \begin{bmatrix} \psi_f \\ 0 \end{bmatrix}, \tag{13}$$

$$\begin{bmatrix} v_d \\ v_q \end{bmatrix} = \begin{bmatrix} R_s + L_d(i_d, i_q) \frac{d}{dt} & -\omega_r L_q(i_d, i_q) \\ \omega_r L_d(i_d, i_q) & R_s + L_q(i_d, i_q) \frac{d}{dt} \end{bmatrix} \begin{bmatrix} i_d \\ i_q \end{bmatrix} + \omega_r \psi_f \begin{bmatrix} 0 \\ 1 \end{bmatrix}, \tag{14}$$

$$T_e = \frac{3Z_r}{2} (\psi_f i_q + (L_d - L_q) i_d i_q). \tag{15}$$

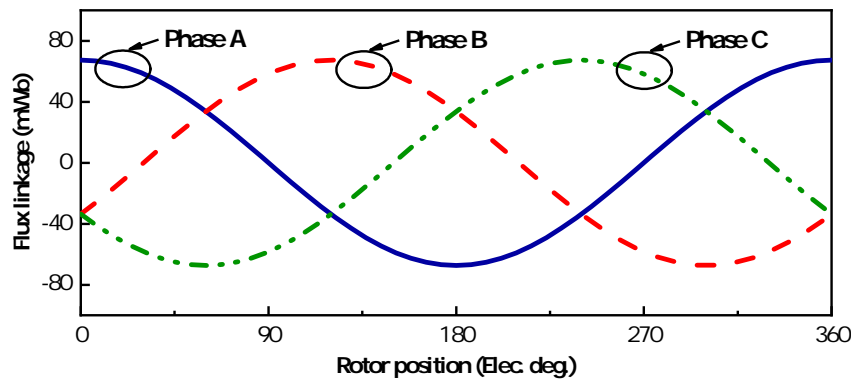


Figure 7. Open-circuit three phase flux linkage.

The other detailed parameters are given in Table 2.

**Table 2.** Main Electromagnetic Parameters of the Proposed Machine.

Parameters	Value
Stator resistance	0.34 Ω
d-axis inductance	7.1–12 mH
q-axis inductance	9.1–11.1 mH
Excitation flux linkage	0.067 Wb
Rated speed	600 rpm
Open-circuit back-EMF	29.2 V
Rated current	5.2 A
Rated torque	3 Nm
Electrical period	7

**4. Structure of Field-Oriented Control System**

The whole sensorless control system is shown in Figure 8. As can be seen, the proposed machine is driven by a three-phase inverter, whose switching signals comes from a SVPWM generator. The sampling circuit collects the two-phase current signals. The CLARKE and PARK transformation modules transfer the phase current into synchronous current, during which the rotor speed and position are estimated by the MRAS method. The expected  $i_q$  is generated by the speed loop, and the expected  $i_d$  is defined by the user. The current loop generates the expected synchronous voltage, which is transferred to the static coordinate as the input of the SVPWM generator. In this paper, the  $i_d = 0$  current control strategy is adopted. The switching frequency of IGBTs is 10kHz. Additionally, the inductance  $L_d$  and  $L_q$  are generated by the inductance estimation module.

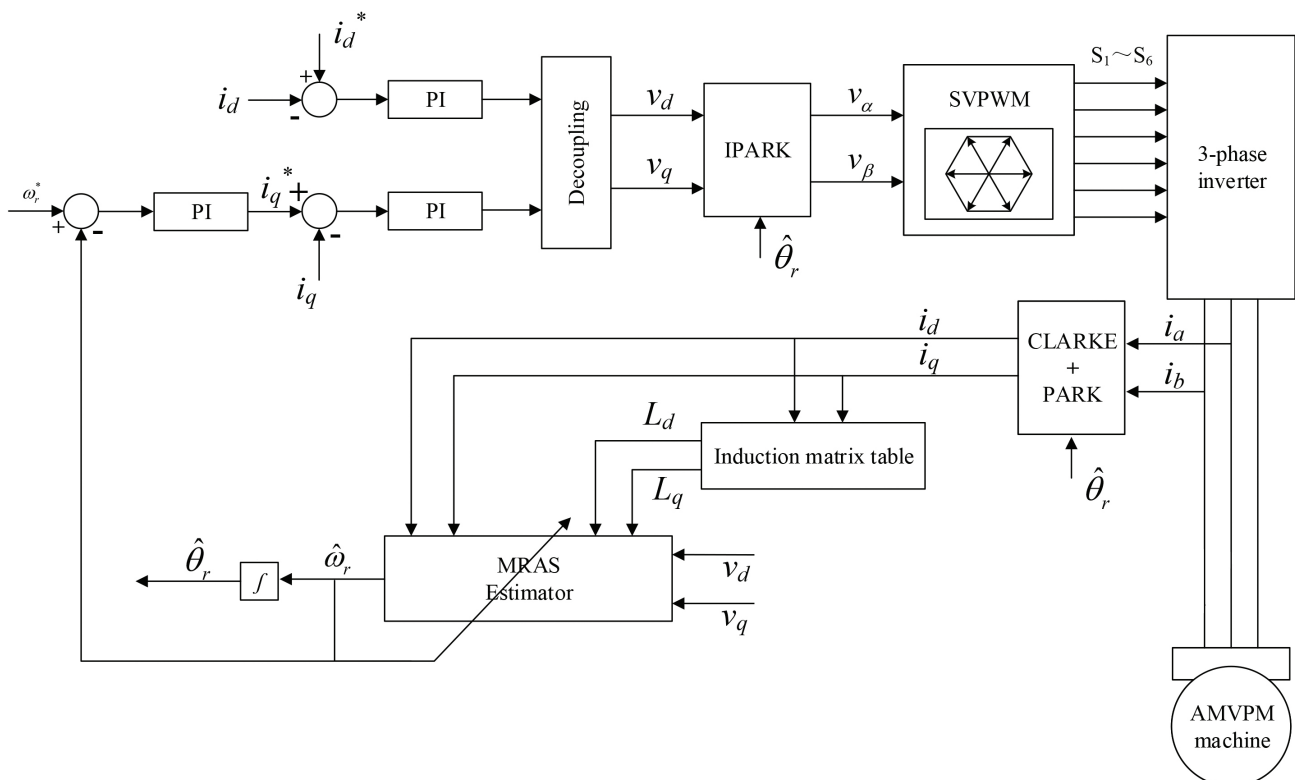


**Figure 8.** The global sensorless vector control system diagram.

The estimated speed is developed by the MRAS method. The main feature of the MRAS method is to use a reference model to specify the required performance of the system. The method mainly includes a reference model and an adjustable model. Among them, the

reference model and the adjustable model are excited by the same input and each produce a response. The difference in their responses reflects the errors in certain parameters in the adjustable model. This response adjusts the parameters of the adjustable model through the adaptive law, so that the response of the adjustable model can approximate the reference model. The structure of MRAS is shown in Figure 9, where the reference model is designed based on (13):

$$\frac{d}{dt}[X] = [A][X] + [B][U] + [C], \tag{16}$$

where

$$[X] = \begin{bmatrix} i_d \\ i_q \end{bmatrix}, [A] = \begin{bmatrix} -\frac{R_s}{L_d} & \frac{L_q}{L_d} \omega_m \\ -\frac{L_d}{L_q} \omega_m & -\frac{R_s}{L_q} \end{bmatrix}, \tag{17}$$

$$[B] = \begin{bmatrix} \frac{1}{L_d} & 0 \\ 0 & \frac{1}{L_q} \end{bmatrix}, [U] = \begin{bmatrix} v_d \\ v_q \end{bmatrix}, [C] = \begin{bmatrix} 0 \\ -\frac{\psi_f}{L_q} \omega_m \end{bmatrix}.$$

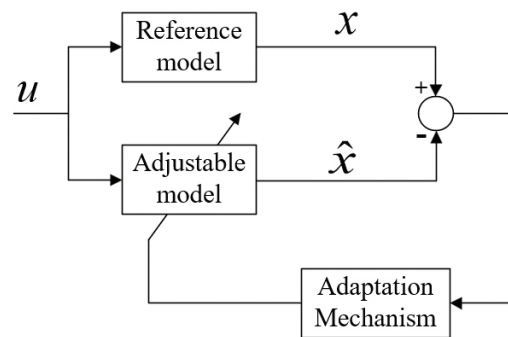


Figure 9. Diagram of MRAS estimation method.

The adjustable model is designed as:

$$\begin{bmatrix} v_d \\ v_q \end{bmatrix} = \begin{bmatrix} R_s + \frac{d}{dt}L_d(i_d, i_q) & -\hat{\omega}_r L_q(i_d, i_q) \\ \hat{\omega}_r L_d(i_d, i_q) & R_s + \frac{d}{dt}L_q(i_d, i_q) \end{bmatrix} \begin{bmatrix} \hat{i}_d \\ \hat{i}_q \end{bmatrix} + \hat{\omega}_r \psi_f \begin{bmatrix} 0 \\ 1 \end{bmatrix}. \tag{18}$$

It is worth mentioning the current changes with high frequency and small amplitude, so the inductance can be taken as constant in (18).

Subtracting (18) by (14), the stator current error can be expressed by:

$$\frac{d}{dt} \begin{bmatrix} e_d \\ e_q \end{bmatrix} = \begin{bmatrix} -\frac{R_s}{L_d} & \hat{\omega}_r \frac{L_q}{L_d} \\ -\hat{\omega}_r \frac{L_d}{L_q} & -\frac{R_s}{L_q} \end{bmatrix} \begin{bmatrix} e_d \\ e_q \end{bmatrix} + \begin{bmatrix} \frac{L_q}{L_d} \hat{i}_q \\ -\frac{L_d}{L_q} \hat{i}_d - \frac{\psi_f}{L_q} \end{bmatrix} (\omega_r - \hat{\omega}_r). \tag{19}$$

The state error model of the proposed machine can be written as:

$$\frac{d}{dt}[e] = [A_e][e] + (\hat{\omega}_r - \omega_r)J[\hat{\Phi}], \tag{20}$$

where

$$[e] = \begin{bmatrix} e_d \\ e_q \end{bmatrix}, [A_e] = \begin{bmatrix} -\frac{R_s}{L_d} & \hat{\omega}_r \frac{L_q}{L_d} \\ -\hat{\omega}_r \frac{L_d}{L_q} & -\frac{R_s}{L_q} \end{bmatrix}, \tag{21}$$

$$[J] = \begin{bmatrix} 0 & -1 \\ 1 & 0 \end{bmatrix}, [\hat{\Phi}] = \begin{bmatrix} \frac{L_d}{L_q} \hat{i}_d + \frac{\psi_f}{L_q} \\ \frac{L_q}{L_d} \hat{i}_q \end{bmatrix}.$$

The equivalent non-linear feedback system is illustrated in Figure 10. According to the Popov hyperstability theory, two conditions needs to be satisfied to prove that the system is asymptotically stable. (a) The linear time-invariant forward path transfer matrix (the

gray part) is strictly positive real; (b) The nonlinear feedback element (all the other part) must satisfy the following equation:

$$\eta(0, t_1) = \int_0^{t_1} [e]^T (\hat{\omega}_r - \omega_r) J[\hat{\Phi}] dt \geq -r_0^2. \tag{22}$$

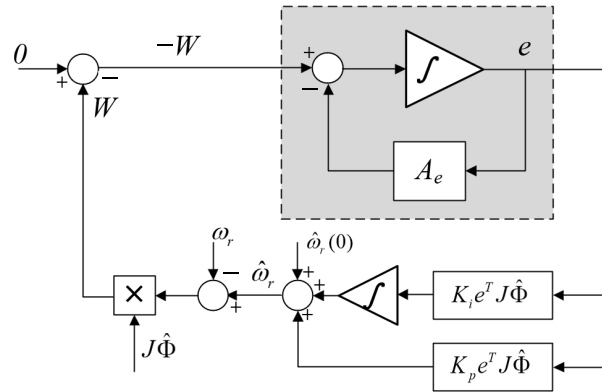


Figure 10. Equivalent non-linear feedback system.

The first condition can be easily proved by the root locus plot of forward path transfer matrix  $(s[I] - [A])^{-1}$ , which is shown in Figure 11. As is shown, the root locus of the forward path transfer matrix moves within the green area, taking into account the changes of  $L_d, L_q$ , and  $\omega_r$ .

To prove the second condition,  $\hat{\omega}_r$  can be set as:

$$\hat{\omega}_r = \int_0^{t_0} K_i [e]^T J[\hat{\Phi}] dt + K_p [e]^T J[\hat{\Phi}] + \hat{\omega}_r(0). \tag{23}$$

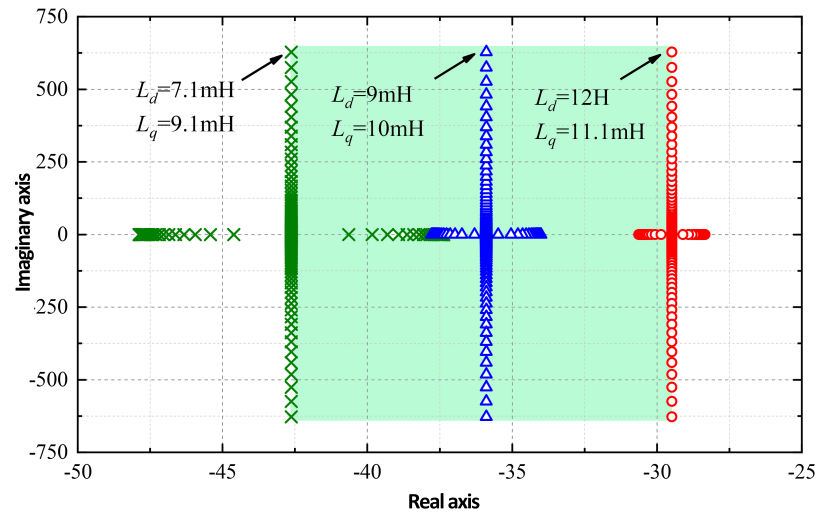


Figure 11. Poles loci for forward path transfer matrix.

Substituting (23) into (22), the inequation becomes:

$$\begin{aligned} \eta(0, t_1) = & \int_0^{t_1} [e]^T \left( \int_0^{t_0} K_i [e]^T J[\hat{\Phi}] d\tau + \hat{\omega}_r(0) - \omega_r \right) J[\hat{\Phi}] dt \\ & + \int_0^{t_1} [e]^T K_p [e]^T J[\hat{\Phi}] dt \geq -r_0^2, \end{aligned} \tag{24}$$

which can be deduced by proving

$$\int_0^{t_1} [e]^T \left( \int_0^{t_0} K_i [e]^T J[\hat{\Phi}] d\tau + \hat{\omega}_r(0) - \omega_r \right) J[\hat{\Phi}] dt \geq -r_1^2 \tag{25}$$

$$\int_0^{t_1} [e]^T K_p [e]^T J[\hat{\Phi}] dt \geq -r_2^2. \tag{26}$$

Equation (25) can be proved by

$$\int_0^{t_1} \frac{df(t)}{dt} kf(t) dt = \frac{k}{2} (f^2(t_1) - f^2(0)) \geq \frac{1}{2} kf^2(0), \tag{27}$$

where

$$\frac{df(t)}{dt} = [e]^T J[\hat{\Phi}], \tag{28}$$

$$kf(t) = \int_0^{t_0} K_i [e]^T J[\hat{\Phi}] d\tau + \hat{\omega}_r(0) - \omega_r. \tag{29}$$

It can be found that (28) is the differential result of (29).

Additionally, (26) can be easily proved if  $K_p > 0$ . In conclusion, the adaptive law (23) is proved to be asymptotically stable. Meanwhile, it is obtained that  $\hat{\omega}_r$  can be estimated as:

$$\hat{\omega}_r = k_p D + \frac{k_i}{s} D, \tag{30}$$

$$D = \frac{L_q}{L_d} i_q e_d - \frac{L_d}{L_q} i_d e_q - \frac{\psi_f}{L_q} e_q. \tag{31}$$

Since  $\hat{\omega}_r$  and  $\omega_r$  are time-varying, it is necessary to investigate the dynamic response of MRAS estimation loop [20]. After linearizing the block in Figure 10, the linearized transfer function of  $\frac{\Delta e}{\Delta \hat{\omega}_r}$  can be expressed as:

$$\frac{D}{\Delta \hat{\omega}_r} \Big|_{\Delta \omega_r=0} = G_p = \frac{\left( \left( \frac{\varphi_d}{L_q} \right)^2 + \left( \frac{\varphi_q}{L_d} \right)^2 \right) s + \frac{1}{t_d} \left( \frac{\varphi_d}{L_q} \right)^2 + \frac{1}{t_q} \left( \frac{\varphi_q}{L_d} \right)^2 + \left( 1 - \left( \frac{L_q}{L_d} \right)^2 \right) \frac{\varphi_d}{L_q} i_q \hat{\omega}_r}{\left( s + \frac{1}{t_d} \right) \left( s + \frac{1}{t_q} \right) + \hat{\omega}_r^2}, \tag{32}$$

where

$$\varphi_d = L_d i_d + \varphi_f, \tag{33}$$

$$\varphi_q = L_q i_q, \tag{34}$$

$$t_d = \frac{L_d}{R_s}, \tag{35}$$

$$t_q = \frac{L_q}{R_s}. \tag{36}$$

Therefore, Figure 10 can be simplified to Figure 12

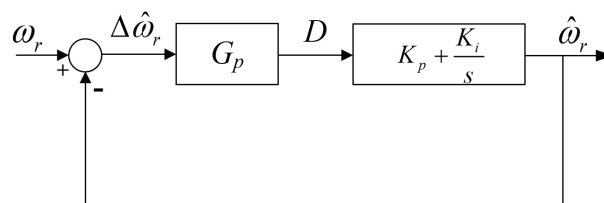


Figure 12. Simplified scheme of speed estimation.

Substitute the parameters in Table 2 into (32), and set the PI controller as  $K_p = 20$ ,  $K_i = 10,000$ , the root locus of the closed-loop poles is shown in Figure 13. As can be seen, when the mechanical speed changes from 0.1 rpm to 1200 rpm, a pair of poles finally stabilize at  $-524$ . Another pole is very close to the imaginary axis, and gradually approaches the imaginary axis as the speed increases. The influence of this pole can be effectively reduced by increasing  $K_i$ . For example, when  $\omega_r$  is 1200 rpm, the real value of this pole is  $-3.79$  when  $K_i$  is 1000, and the real value of this pole is  $-30.1$  when  $K_i$  is 10,000.

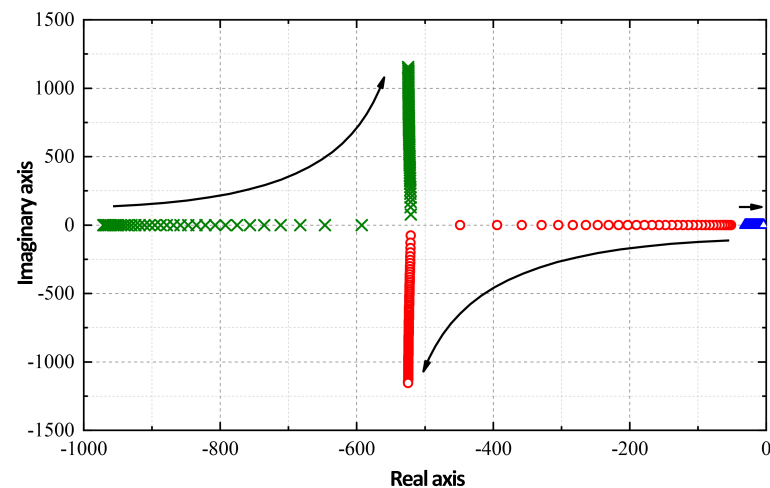


Figure 13. Pole placement of the closed-loop transfer function of speed estimation.

## 5. Simulation Results

In this section, the simulation calculation is carried out based on the Matlab\Simulink software to verify the feasibility of the designed control strategy. The designed test process is that the initial motor speed is 600 rpm and the load torque is 1.5 Nm (half load). The rotational speed increases with a fixed slope from 1 s and rises to 800 rpm at 1.5 s and remains unchanged. The load torque is switched from 1.5 Nm to 3 Nm (full load) at 2.5 s. During 4 s and 5 s, the speed drops from 800 rpm to 400 rpm.

It can be seen from Figure 14 that the estimated speed is very close to the reference speed. It is worth mentioning that the speed fluctuation looks a little larger than the general simulation results. It is because the proposed machine is a Vernier machine. The stator inductance is inherently larger than normal PMSM, so the stator time constant is quite larger. Therefore, the response speed of proposed machine will be slower. From Figure 14b, it is found that the speed estimation error is around 20rpm. The estimation error at rated speed is  $\pm 3.3\%$ , which is acceptable.

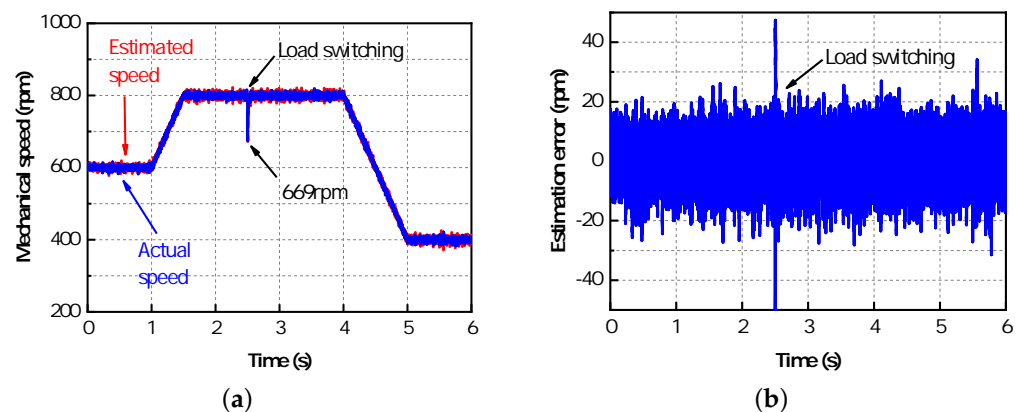
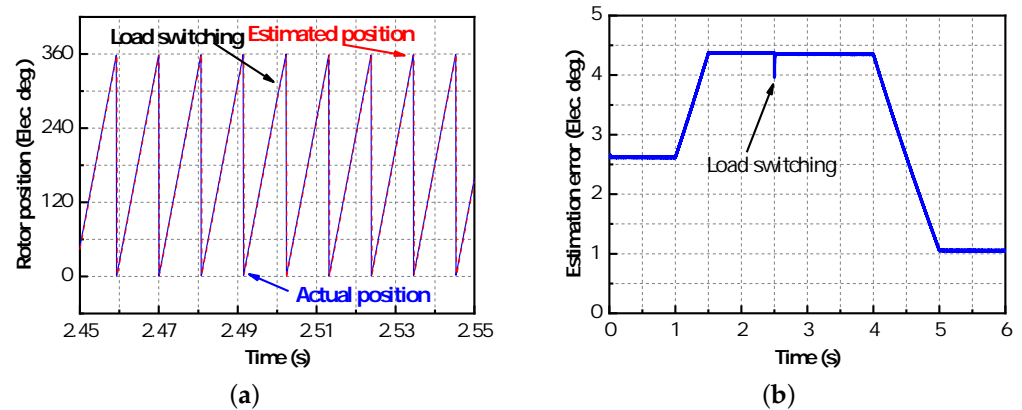


Figure 14. Simulation results of speed using the inductance matrix table. (a) Estimated speed and (b) estimation error.

Figure 15 shows the estimated and actual electrical rotor position. As can be seen, the estimated position is of high accuracy. The waveform of position estimation error is similar with that of the speed. It is because the estimated position is obtained by integrating the estimated speed, and there is one-cycle delay between the estimated speed and the real speed. The error might be eliminated by algorithmic compensation, which will not be discussed in this paper.



**Figure 15.** Simulation results of rotor position using the inductance matrix table. (a) Rotor position and (b) estimation error.

The d- and q-axis current is given in Figure 16. The reference value of  $i_d$  is 0, and the reference value of  $i_q$  is generated from the speed loop. The simulation results show that the performance of the current loop is very good. Finally, Figure 17 shows the estimated inductance during the control process. Since the current loop has satisfactory performance, the ripple of the current is very small. Therefore, in most of time, the inductance is a constant.

For comparison, both the d- and q-axis inductance are fixed at 10 mH in the following simulation to investigate the control performance without non-linear inductance matrix, during which the inductance in machine model is still current-dependent. The test process is the same, and the simulation results are shown in Figures 18–20. It can be seen that both the speed fluctuation and the estimation error are much larger. The same problem is found in rotor position estimation error and the current fluctuation. It is verified that the addition of inductance estimation can improve the performance of the control strategy.

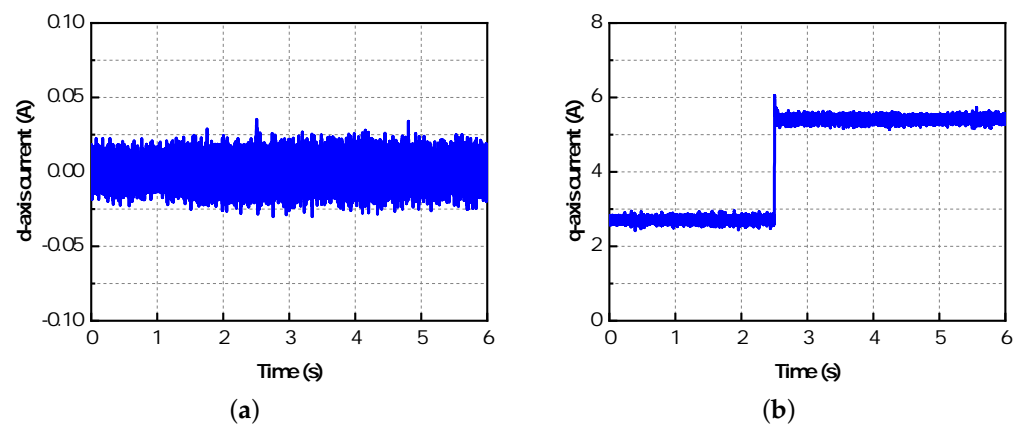


**Figure 16.** Simulation results of current using the inductance matrix table. (a) d-axis current and (b) q-axis current.

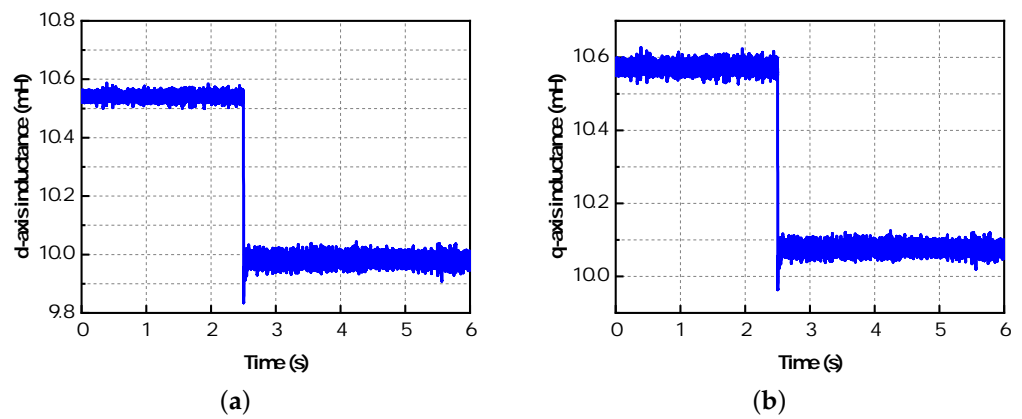


Figure 17. Estimated inductance according to the inductance matrix table. (a) d-axis inductance and (b) q-axis inductance.

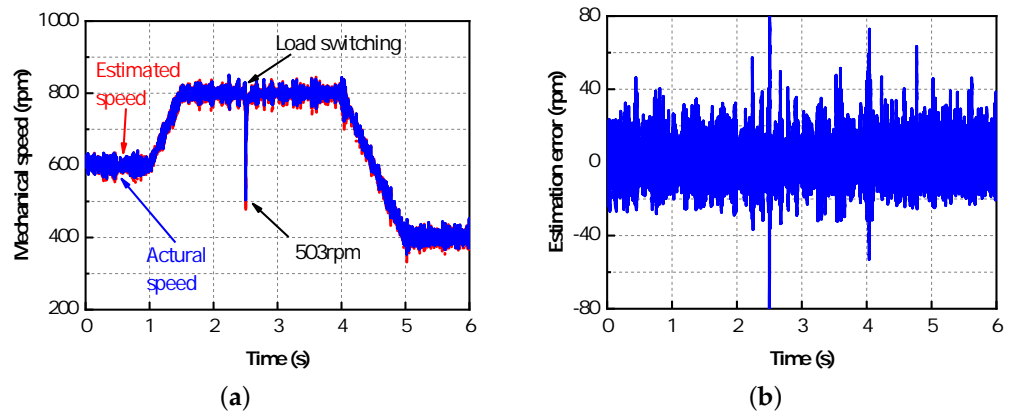


Figure 18. Simulation results of speed using the constant inductance. (a) Estimated speed and (b) estimation error.

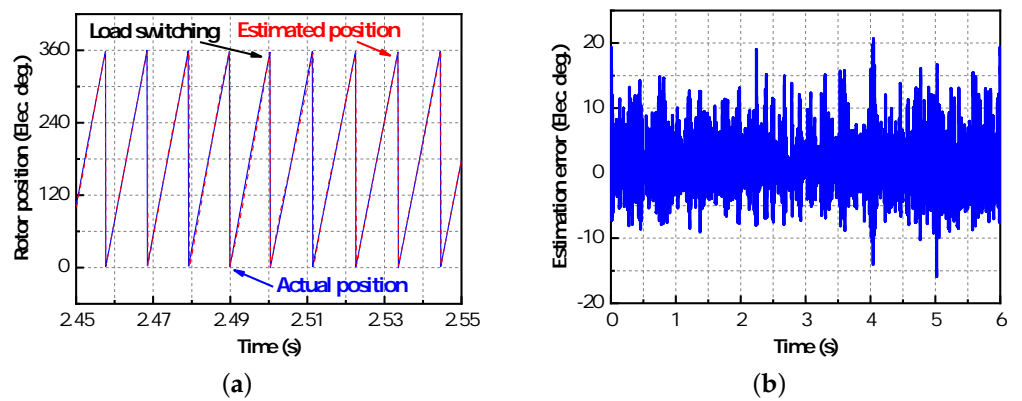
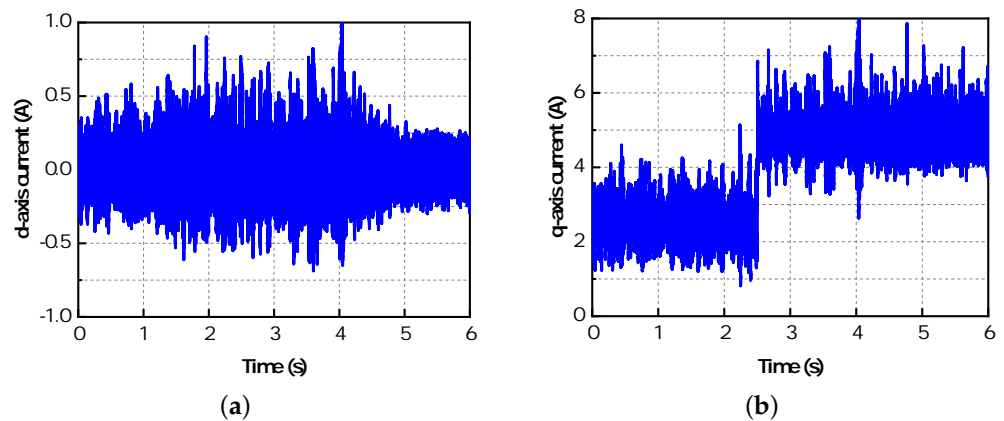


Figure 19. Simulation results of rotor position using the constant inductance. (a) Rotor position and (b) estimation error.



**Figure 20.** Simulation results without inductance estimation. (a) d-axis current and (b) q-axis current.

To further investigate the performances of proposed control method on AMVPM machine, an extended EMF-based sensorless control system is also built in the SIMULINK software according to [28]. For fair comparison, the inductance table is also used for inductance estimation.

The speed results are shown in Figure 21, and the rotor position results are shown in Figure 22. From Figure 22b it can be seen that, since the extended EMF-based method focuses on the rotor position (the estimated speed is determined by the position error), its position error is smaller than that of the proposed method. However, as shown in Figure 21b, since the estimated speed is no longer traced, the speed estimation error is larger than that of the proposed method. It is noticed in Figure 21a that the actual speed has a static error of nearly 30 rpm, which is not desired. The phenomenon that the rotor position error is proportional to the speed can also be found in the extended EMF-based method.

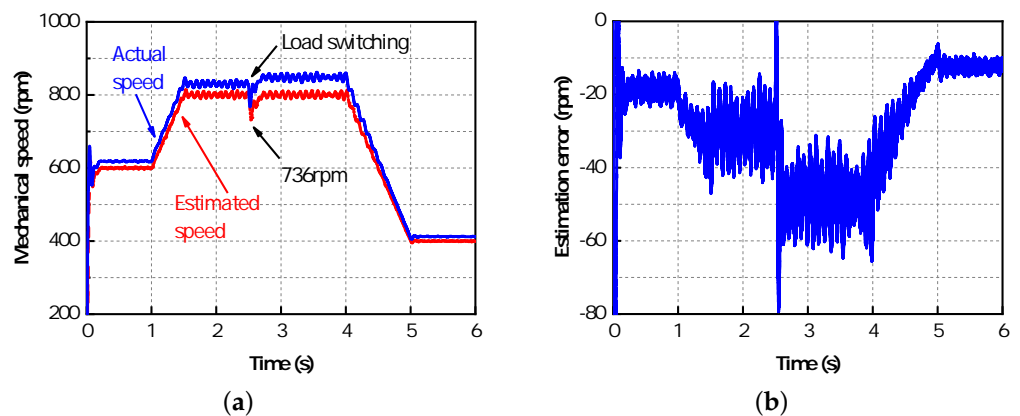


**Figure 21.** Simulation results of speed by extended EMF-based method. (a) Estimated speed and (b) estimation error.

Overall, the simulation results show great performance of the MRAS-based sensorless control system for the proposed AMVPM machine. It validates the feasibility of the designed control strategy for real-time working condition.

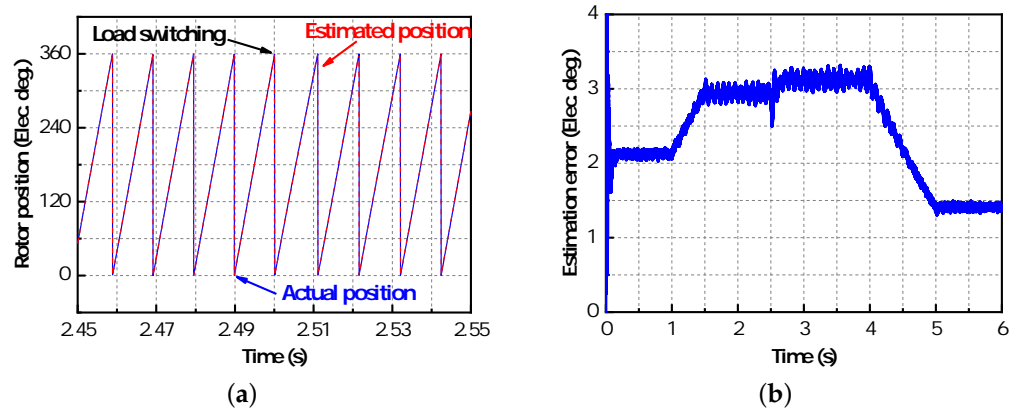


**Figure 22.** Simulation results of rotor position by extended EMF-based method. (a) Rotor position and (b) estimation error.

## 6. Experiment Validation

In order to verify the previous analysis, a test bench is built up as shown in Figure 23. Additionally, the TI HVMTRPFCKIT with TMS320F28335 microcontroller is selected as the inverter, as can be seen in Figure 24. The switching frequency is 10 kHz which is the same as in the simulation. The dead-time is set to 2  $\mu$ s.

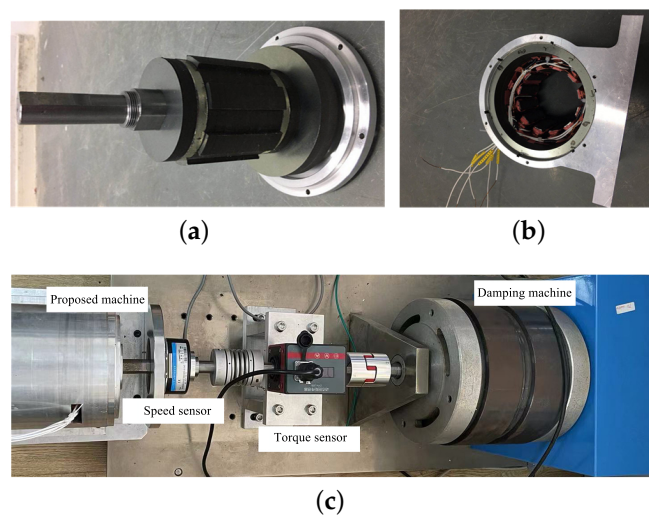


**Figure 23.** Prototype of the proposed machine. (a) Stator; (b) rotor; and (c) test bench.



**Figure 24.** TI HVMTRPFCKIT inverter.

The results of speed estimation performance are shown in Figure 25. It is found that the experiment results are basically consistent with the simulation results. It is noted that in the experiment process there is no speed drop when the load is switched. It is because the magnetic powder dynamometer on the test bench needs to adjust the load manually, the load switching process is not instantaneous. Therefore, the speed loop has enough time to maintain the reference speed. The rotor estimation error in Figure 26 is larger than the simulation results. The main reason is that there are problems, such as motor parameter error, shaft rotation fluctuation, and unsatisfactory controller switch, during the experiment.

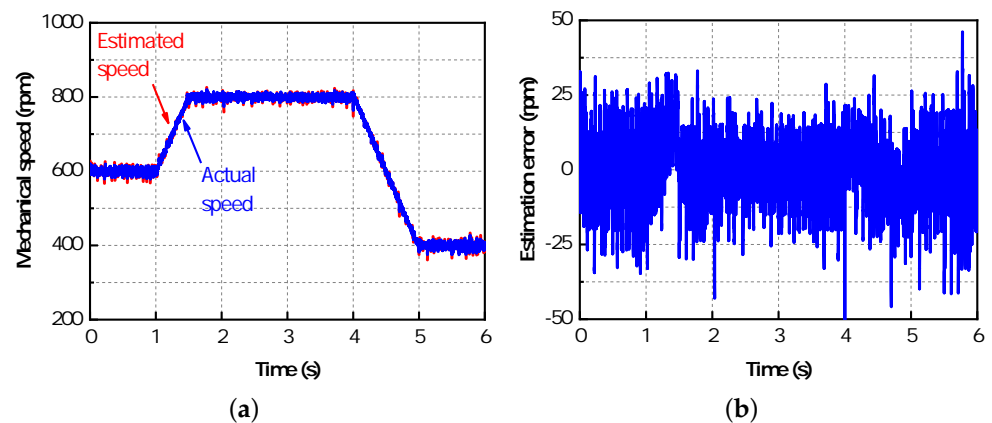


Figure 25. Experimental results.(a) Estimated speed and (b) estimation error.

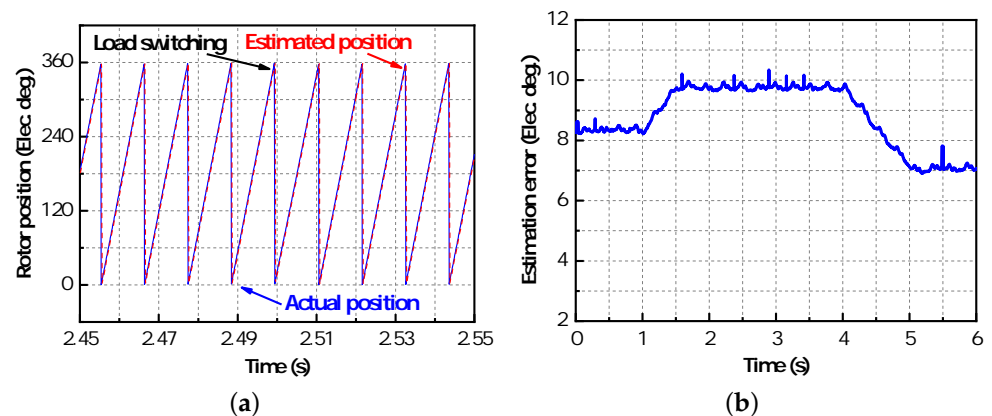
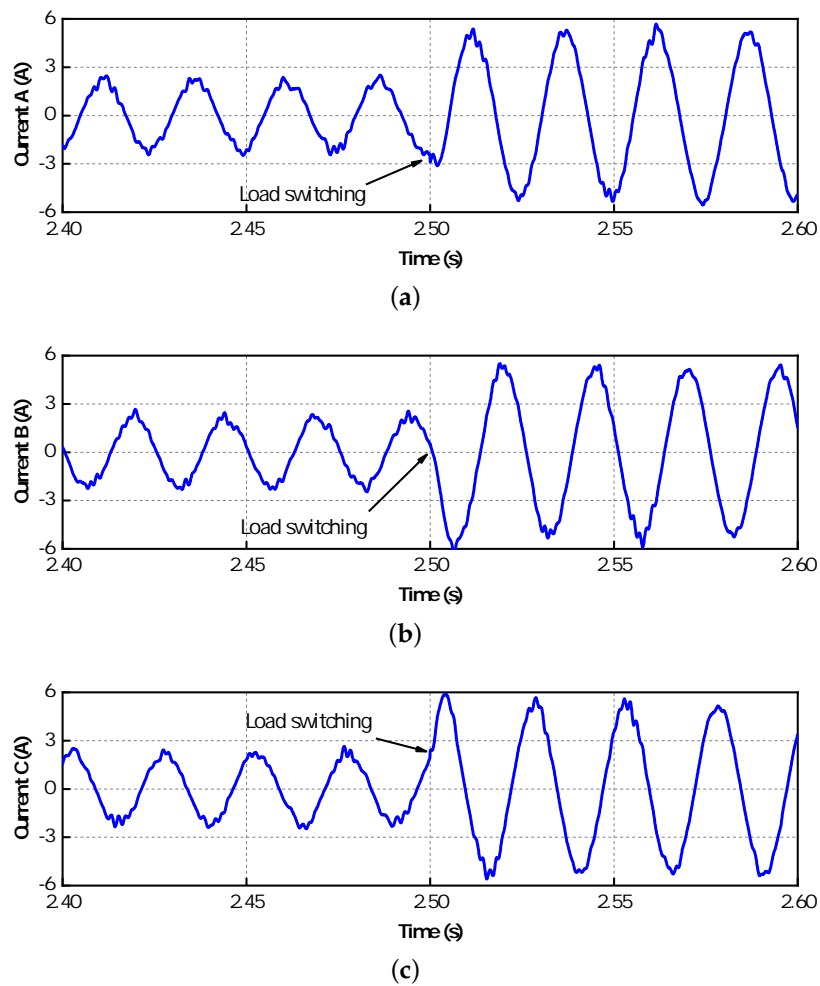
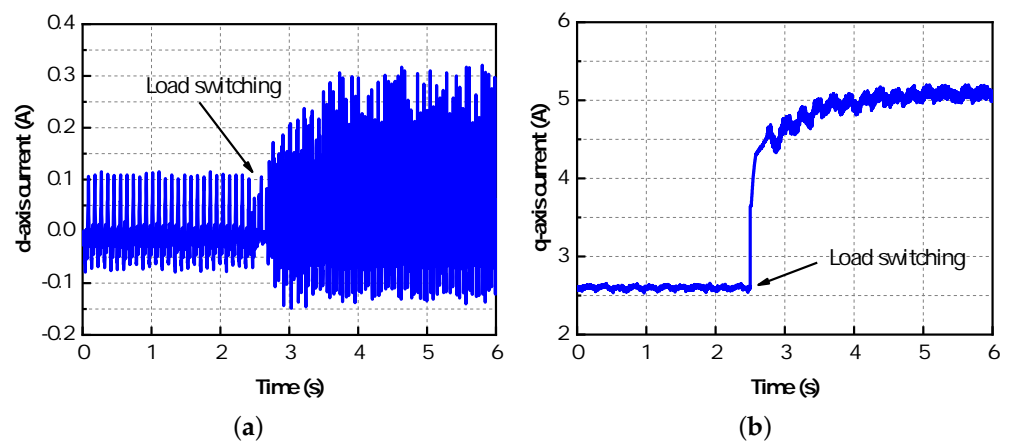


Figure 26. Experimental results.(a) Rotor position and (b) estimation error.

The current results are shown in Figures 27 and 28. It can be seen from Figure 28 that the d-axis current has a larger glitch after the load is switched. This is mainly due to the coupling between  $L_d \frac{d}{dt} i_d$  and  $L_q i_q$  in the first line of (14). After the load is switched,  $i_q$  becomes larger. Although it can be balanced with larger  $V_d$ , the ripple of  $i_q$  still increases, which results in larger ripple of  $i_d$ . In Figure 28b, the response process of the q-axis current after load switching is also slower than the simulation results. It is also because the magnetic powder dynamometer needs to be adjusted manually. The q-axis current values under half-load and full-load conditions are basically consistent with the simulation results. It can be seen from Figure 27 that when the load torque changes, the adjustment is completed within the 2 electrical periods, reflecting the excellent dynamic performance of the control algorithm.



**Figure 27.** Experimental results.(a) Phase A current; (b) Phase B current; and (c) Phase C current.



**Figure 28.** Experimental results.(a) d-axis current and (b) q-axis current.

Figure 29 shows the estimated value of the stator inductance. Since the q-axis current increases after the load is switched, the saturation degree of the iron core increases. Therefore, the inductance of the d-axis and q-axis decreases.

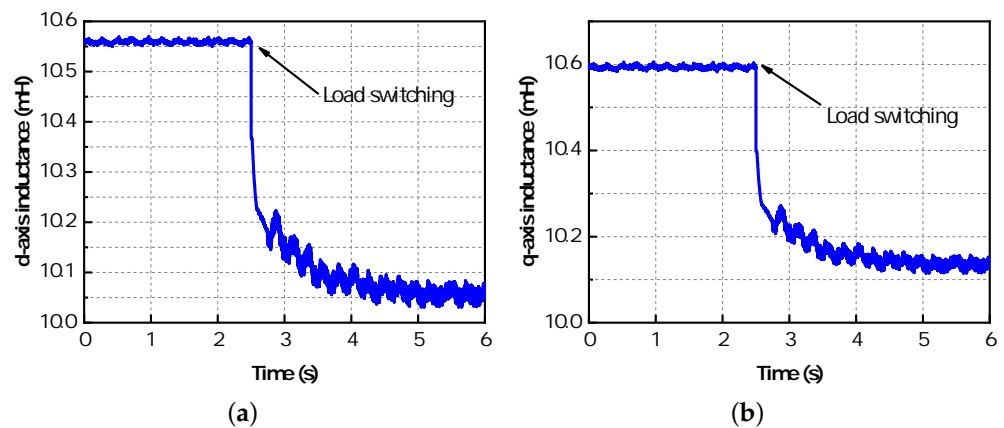


**Figure 29.** Experimental results. (a) d-axis inductance and (b) q-axis inductance.

The experiment with constant inductance value is also conducted. It is found that the machine cannot normally rotate. The results once again proved the necessity of combining inductance matrix table with the MRAS estimator.

Overall, the good agreement between the FE model and the manufacturing prototype has been validated.

## 7. Discussion

In this paper, the inductance non-linearity of the axially magnetized VPM machine under different combinations of d-axis and q-axis currents is investigated. An improved MRAS identification technique for the proposed machine is presented. The electromagnetic characteristic of the proposed machine is calculated. The state equation of the machine is established according to the offline-calculated inductance matrix and other parameters. The simulation results show great performances of the whole system. Finally, the machine prototype, as well as the control system platform, are manufactured, and the simulation conclusions are experimentally validated.

**Author Contributions:** Conceptualization, Y.F. and B.X.; methodology, J.M.; software, Q.W.; validation, J.M., B.X. and Q.W.; formal analysis, C.L.; investigation, L.Q.; resources, Q.W.; data curation, B.X.; writing—original draft preparation, B.X.; writing—review and editing, X.L.; visualization, X.L.; supervision, B.X.; project administration, J.M.; funding acquisition, Y.F. All authors have read and agreed to the published version of the manuscript.

**Funding:** This research was funded by National Natural Science Foundation of China, Grant Number 51977193, 51827810.

**Institutional Review Board Statement:** Not applicable.

**Informed Consent Statement:** Not applicable.

**Data Availability Statement:** The data presented in the paper are available upon request from the corresponding author (J.M.).

**Conflicts of Interest:** The authors declare no conflict of interest.

## References

- Ishizaki, A.; Tanaka, T.; Takasaki, K.; Nishikata, S. Theory and optimum design of PM Vernier motor. In Proceedings of the 7th International Conference on Electrical Machines and Drives, Durham, UK, 11–13 September 1995; pp. 208–212.
- Li, D.; Qu, R.; Lipo, T. A. High-Power-Factor Vernier Permanent-Magnet Machines. *IEEE Trans. Ind. Appl.* **2014**, *50*, 3664–3674. [[CrossRef](#)]
- Jang, D.; Chang, J. Design of a Vernier Machine With PM on Both Sides of Rotor and Stator. *IEEE Trans. Magn.* **2014**, *50*, 877–880. [[CrossRef](#)]
- Li, D.; Qu, R.; Li, J.; Xu, W. Design of consequent pole toroidal winding outer rotor Vernier permanent magnet machines. In Proceedings of the 2014 IEEE Energy Conversion Congress and Exposition, Pittsburgh, PA, USA, 14–18 September 2014; pp. 2342–2349.

5. Kim, B.; Lipo, T.A. Operation and design principles of a PM Vernier motor. *IEEE Trans. Ind. Appl.* **2014**, *50*, 3656–3663. [[CrossRef](#)]
6. Liao, Y.; Liang, F.; Lipo, T.A. A novel permanent magnet motor with doubly salient structure. *IEEE Trans. Ind. Appl.* **1995**, *3*, 1069–1078. [[CrossRef](#)]
7. Cheng, M.; Chau, K.T.; Chau, C.C.; Zhou, E.; Huang, X. Nonlinear varying-network magnetic circuit analysis for doubly salient permanent-magnet motors. *IEEE Trans. Magn.* **2000**, *36*, 339–348. [[CrossRef](#)]
8. Cheng, M.; Chau, K.T.; Chau, C.C. Design and analysis of a new doubly salient permanent magnet motor. *IEEE Trans. Magn.* **2001**, *37*, 3012–3020. [[CrossRef](#)]
9. Hua, W.; Zhu, X.; Wu, Z. Influence of coil pitch and stator-slot/rotor-pole combination on back EMF harmonics in flux-reversal permanent magnet machines. *IEEE Trans. Energy Convers.* **2018**, *33*, 1330–1341. [[CrossRef](#)]
10. Li, H.; Zhu, Z. Influence of magnet arrangement on performance of flux reversal permanent magnet machine. In Proceedings of the 2017 IEEE International Electric Machines and Drives Conference, Miami, FL, USA, 21–24 May 2017; pp. 1–8.
11. Li, H.; Zhu, Z. Optimal number of magnet pieces of flux reversal permanent magnet machines. *IEEE Trans. Energy Convers.* **2019**, *34*, 889–898. [[CrossRef](#)]
12. Rauch, S.E.; Johnson, L.J. Design principles of flux-switching alternators. *AIEE Trans. Power Appl. Syst.* **1955**, *74*, 1261–1268.
13. Chen, J.; Zhu, Z.; Iwasaki, S.; Deodhar, R.P. A novel E-core switched-flux PM brushless ac machine. *IEEE Trans. Ind. Appl.* **2011**, *47*, 1273–1282. [[CrossRef](#)]
14. Zhu, Z.; Chen, J.; Pang, Y.; Howe, D.; Iwasaki, S.; Deodhar, R. Analysis of a novel multi-tooth flux-switching PM brushless ac machine for high torque direct-drive applications. *IEEE Trans. Magn.* **2008**, *44*, 4313–4316. [[CrossRef](#)]
15. Xu, B.; Wu, L.; Ma, J.; Pierre, D.P.; Huang, X.; Qiu, L.; Fang, Y. A Novel Axially Magnetized Vernier Permanent-Magnet Machine. *IEEE Trans. Magn.* **2021**, *57*, 1–5. [[CrossRef](#)]
16. Xu, B.; Ma, J.; Wu, L.; Huang, X.; Fang, Y. Investigation of Novel Axially Magnetized Vernier Permanent-Magnet Machine in Cascade Structure. In Proceedings of the 23rd International Conference on Electrical Machines and Systems, Hamamatsu, Japan, 24–27 November 2020; pp. 1246–1250.
17. Jang, J.; Ha, J.; Ohto, M.; Ide, K.; Sul, S. Analysis of permanent-magnet machine for sensorless control based on high-frequency signal injection. *IEEE Trans. Ind. Appl.* **2004**, *40*, 1595–1604. [[CrossRef](#)]
18. Liu, J.; Zhu, Z. Novel Sensorless Control Strategy With Injection of High-Frequency Pulsating Carrier Signal Into Stationary Reference Frame. *IEEE Trans. Ind. Appl.* **2014**, *50*, 2574–2583. [[CrossRef](#)]
19. Caruana, C.; Asher, G.; Sumner, M. Performance of HF signal injection techniques for zero-low-frequency vector control of induction Machines under sensorless conditions. *IEEE Trans. Ind. Electron.* **2006**, *53*, 225–238. [[CrossRef](#)]
20. Schauder, C. Adaptive speed identification for vector control of induction motors without rotational transducers. *IEEE Trans. Ind. Appl.* **1992**, *28*, 1054–1061. [[CrossRef](#)]
21. Rashed, M.; MacConnell, P.; Stronach, A.; Acarnley, P. Sensorless indirect-rotor-field-orientation speed control of a permanent-magnet synchronous motor with stator-resistance estimation. *IEEE Trans. Ind. Electron.* **2007**, *54*, 1664–1675. [[CrossRef](#)]
22. Nahid-Mobarakeh, B.; Meibody-Tabar, F.; Sargos, F. Mechanical sensorless control of PMSM with online estimation of stator resistance. *IEEE Trans. Ind. Appl.* **2004**, *40*, 457–471. [[CrossRef](#)]
23. Mese, E.; Torrey, D.A. An approach for sensorless position estimation for switched reluctance motors using artificial neural networks. *IEEE Trans. Power Electron.* **2002**, *17*, 66–75. [[CrossRef](#)]
24. Shi, Y.; Sun, K.; Huang, L. Online identification of permanent magnet flux based on extended kalman filter for IPMSM drive with position sensorless control. *IEEE Trans. Ind. Electron.* **2012**, *59*, 4169–4178. [[CrossRef](#)]
25. Zhao, Y.; Qiao, W.; Wu, L. Improved rotor position and speed estimators for sensorless control of interior permanent-magnet synchronous machines. *IEEE Trans. Emerg. Sel. Top. Power Electron.* **2014**, *2*, 627–639. [[CrossRef](#)]
26. Solsona, J.; Valla, M.I.; Muravchik, C. A nonlinear reduced order observer for permanent magnet synchronous motors. *IEEE Trans. Ind. Electron.* **1996**, *2*, 492–497. [[CrossRef](#)]
27. Bolognani, S.; Oboe, R.; Zigliotto, M. Sensorless full-digital PMSM drive with EKF estimation of speed and rotor position. *IEEE Trans. Ind. Electron.* **1999**, *2*, 184–191. [[CrossRef](#)]
28. Morimoto, S.; Kawamoto, K.; Sanada, M.; Takeda, Y. Sensorless control strategy for salient-pole PMSM based on extended EMF in rotating reference frame. *IEEE Trans. Ind. Appl.* **2002**, *38*, 1054–1061. [[CrossRef](#)]
29. Heller, B.; Hamata, V. *Harmonic Field Effects in Induction Machines*; Elsevier: Amsterdam, The Netherlands, 1977; pp. 54–67.
30. Gaussens, O.B.; Hoang, E.; Saint-Michel, J.; Manfe, P.; Lecrivain, M.; Gabsi, M. Magnetic field solution in doubly slotted airgap of conventional and alternate field-excited switched-flux topologies. *IEEE Trans. Magn.* **2013**, *49*, 5083–5096. [[CrossRef](#)]